Nanoscale

Accepted Manuscript

This article can be cited before page numbers have been issued, to do this please use: F. Peng and A. Jabbarzadeh, *Nanoscale*, 2025, DOI: 10.1039/D5NR03035H.

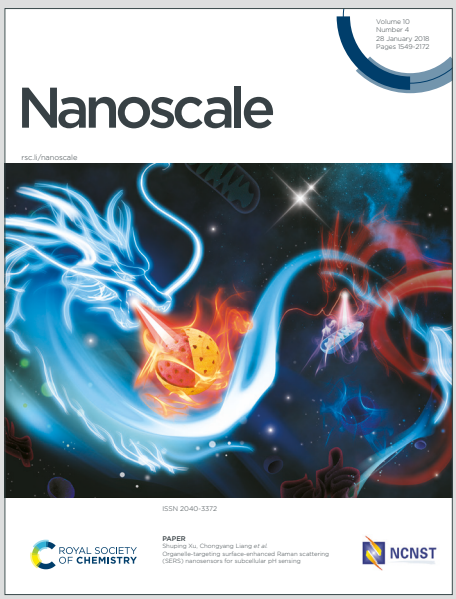

ROYAL SOCIETY OF CHEMISTRY

rsc.li/nanoscale

View Article Online
DOI: 10.1039/D5NR03035H

PAPER

Rheology of Highly Concentrated Bulk Nanobubbles in Water

Fankai Peng[a] and Ahmad Jabbarazadeh*[a]

Received 00th January 20xx,
Accepted 00th January 20xx

DOI: 10.1039/x0xx00000x

Bulk nanobubbles (BNBs), unlike macro bubbles, exhibit extraordinary longevity in water. While their super-stability is well-established, the rheological properties of BNB-water systems remain poorly understood. To address this, we employed molecular dynamics simulations to model nitrogen BNBs with a radius of ~1.9 nm, systematically varying the volume fraction and evaluating the zero-shear viscosity. Our simulations reveal that BNBs exhibit rheological behaviour akin to that of microbubbles, but with a markedly stronger effect. Specifically, the zero-shear viscosity of BNB-water systems exceeds that of pure water and increases significantly with volume fraction—far surpassing the trends observed in microbubble systems. This pronounced increase resembles the behaviour of dilute charged colloidal dispersions, likely due to the high-density gas and surface charges within the nanobubbles. We derived a relative viscosity model grounded in classical theories to describe this behaviour. Under Couette flow, BNBs become unstable at high shear rates, coalescing into larger bubbles. Prior to coalescence, shear viscosity also rises with increasing volume fraction. To validate our findings, we conducted experiments using nanobubbles with a radius of ~70 nm at a high concentration of 4.0×10^{13} bubbles/mL. The experimental data closely matched our simulations: at low shear rates, BNB-water viscosity exceeds that of pure water, while at high shear rates, it drops to baseline levels—likely due to bubble coalescence and gas release. Our experimentally validated model predicts zero-shear viscosity within 8.93% of measured values, underscoring the complex, shear- and concentration-dependent rheology of BNB systems and suggesting current technologies may underestimate actual BNB concentrations.

1 Introduction

Bulk nanobubbles (BNBs) exhibit a range of unique properties—including high concentration, exceptional stability, and strong adsorption capacity—that make them highly attractive for applications such as water treatment, agricultural fertilization and drug delivery.[1-11] While several studies have explored the super-stability of BNBs under static, quiescent conditions[12-15], the rheological characteristics of nanobubble-laden water systems remain poorly understood. In particular, key questions remain unanswered: How do nanobubbles influence the viscosity of water? How does their concentration affect this behaviour? Moreover, how do BNBs respond to flow and deformation in dynamic environments? The lack of studies to address these issues leaves a significant gap in our understanding of the rheological behaviour of nanobubble-rich systems. A comprehensive investigation into the rheology of highly concentrated BNB suspensions is urgently needed. Such insights are critical not only for advancing fundamental science but also for optimizing the performance of BNBs in real-world applications where fluids are often subjected to varying shear conditions. Understanding how BNBs behave under the flow will help bridge the gap between their known static properties and their dynamic performance in practical systems.

Senthilkumar *et al.*[16] studied the viscosity of nanobubbles in various solutions via experiments. However, due to the limitation of nanobubble experiments, the concentration of their nanobubbles was unknown for these ~60-80 nm nanobubbles. Their work suggested a slight decrease in viscosity. On the other hand, some researchers have reported only the rheological behaviours of micro-bubbles rather than nanobubbles.[17-22] These works have studied these systems at low-volume fractions in a viscous fluid such as corn syrup, silicon oil, or even molten magma. Such an approach allows studies over a wide range of capillary numbers ($1 << Ca$ or $Ca << 1$). These works generally suggest an increase in viscosity at low shear rates, where capillary forces are dominant compared to viscous forces, and shear thinning at higher shear rates due to bubble deformation. Hong *et al.*[23] calculated the viscosities of a single BNB in water by using all-atom molecular simulations. Their work treated the nanobubble as a cavity rather than a realistic gas nanobubble. They found that the viscosity of these cavity-laden water systems was lower than that of pure water. However, recent works and our own simulations24 have shown that nanobubbles contain high-density gas. The rheological behaviour of dense BNBs may differ from that of large bubbles or those with low-density gas or cavities. The high-density gas in the nanobubble is explained by Young-Laplace's Law, which states that the pressure difference inside and outside the bubble (ΔP) is equal to $2\Gamma/R$, where Γ is the liquid's surface tension and R is the bubble's radius. This results in exceptionally high pressure and density inside the nanobubbles, causing the gas molecules to be highly compressed, which may alter the rheological behaviours. The surface of these nanobubbles is negatively charged.[5] Can these dense, small BNBs be treated as colloids? According to

[a] School of Aerospace, Mechanical, and Mechatronic Engineering, University of Sydney, Camperdown, NSW 2006, Australia

Russel *et al*.[25], colloidal dispersion is a solution system with small particles (known as colloids) dispersed in a continuous medium. These particles range from 1 nanometer to 1 micrometre, remain suspended, and interact with the dispersing medium.

Understanding the rheological behaviour of bulk nanobubbles (BNBs)—particularly their zero-shear and shear viscosities—is essential for advancing their practical applications. Zero-shear viscosity describes a fluid's resistance to flow in the absence of external forces[26,25] In contrast; shear viscosity reflects a fluid's resistance to deformation under applied shear[2726,27] For Newtonian fluids like water, shear viscosity remains stable across a broad range of shear rates. These properties are fundamental to distinguishing between Newtonian and non-Newtonian fluids and are especially relevant for colloidal systems, offering critical insights into how BNBs behave under different flow conditions. While extensive research has focused on the stability of BNBs in quiescent conditions,[12–15] and several comprehensive reviews have explored their behaviour without shear,[2,4,5,28] a significant knowledge gap remains. Specifically, it is unclear whether BNBs maintain their stability under high shear rates or at elevated concentrations. Investigating these conditions is crucial, as BNBs may exhibit markedly different rheological responses when subjected to dynamic environments. Addressing this gap will not only deepen our understanding of BNB mechanics but also inform their effective integration into industrial and biomedical systems where shear forces are prevalent.

For 100-200 nm BNBs in experiments using Dynamic Light Scattering (DSL) or Nanoparticle Tracking Analysis (NTA), reported concentrations generally range from 10^8 to 10^9 nanobubbles per mL.[29,30] These techniques have an upper limit of concentration measurement of ~10^9 particles/mL,[31] but higher concentrations of 1.9×10^{13} BNBs per mL are reported for ~50 nm nitrogen nanobubbles using density and dissolved gas content.[32] Therefore, it is challenging to determine their rheological properties and dependence on their concentration through experimental means. However, molecular dynamics (MD) simulation is an alternative tool for studying novel BNB systems, which can provide valuable guidance for future BNB applications such as drug delivery and water treatment. Furthermore, there has been no atomistic simulation of the rheological behaviour of BNB systems for these highly concentrated systems, and the effect of concentration on rheology is lacking. We will consider the rheological behaviour of a system of multiple nanobubbles, rather than a single nanobubble. Here, we will calculate the zero-shear viscosity of nitrogen BNBs in water using the Green-Kubo (GK) method to study the effect of BNBs concentration. Furthermore, we consider the response of these systems to shear to calculate the shear viscosity and assess the effect of shear on the behaviour of nanobubbles using the non-equilibrium molecular dynamics (NEMD) SLLOD method. We also determine the effect of nanobubble concentration on their stability. The GK and SLLOD methods have been used in our previous studies, providing valid results.[33] To complement our simulation findings, we will conduct experimental studies on both air and nitrogen BNBs. These experiments will serve to validate the rheological models developed through molecular dynamics simulations. We will determine nanobubble concentrations using mass-based analysis, providing a quantitative benchmark for comparison. Additionally, we will employ direct measurement techniques to highlight the limitations of current experimental methods in accurately capturing BNB concentrations. This dual approach—combining simulation validation with a critical assessment of measurement accuracy—will provide a more comprehensive understanding of BNB behaviour and help refine both theoretical and experimental methodologies.

2 Methodologies

2.1 Molecular model

In this research, we have simulated nitrogen nanobubbles in water. Here, a 3-site charged nitrogen (N) molecular model is employed, where a zero-mass ghost atom (M) is inserted between two physical nitrogen atoms to make each atom charged while maintaining overall molecular neutrality. The nitrogen molecules are treated as rigid bodies with constant bond lengths of 1.21 Å and N-M-N angle of 180°.[34,35] In addition, the TIP4P(Ewald) water model is utilized to model water molecules with the SHAKE algorithm, which also keeps the water molecules rigid. The bond length of O-H in water molecules is 0.9572 Å, and the H-O-H angle is 104.52°.[36,37] We also validated our 3-site charged nitrogen and the TIP4P(Ewald) water models by comparing the density under *NPT* (constant number of atoms, pressure and temperature) conditions with experimental data, as shown in **Table 1**.

Table 1 Comparison of nitrogen and water densities from simulation (ρ_{sim}) and experimental data (ρ_{exp}) at specified temperature (*T*) and pressure (*P*). The expected experimental density corresponding to the simulation conditions is also provided.

	T (K)	*P* (MPa)	ρ_{sim} (kg/m^3)	ρ_{exp} (kg/m^3)	Accuracy
Charged Nitrogen	270	20	229.82	242.18[38]	5%
TIP4P (Ewald) water	300	0.101	988.74	996[39]	0.73%

A 12-6 Lennard-Jones potential is used to describe the intermolecular interactions shown in **eqn (1)**.[40] Additionally, the Columbic pairwise interactions are described by Columbic potential shown in **eqn (2)**.

$$\phi_{LJ}(r_{ij}) = 4\varepsilon_{ij}\left[\left(\frac{\sigma_{ij}}{r_{ij}}\right)^{12} - \left(\frac{\sigma_{ij}}{r_{ij}}\right)^{6}\right] \quad (1)$$

$$E = \frac{Cq_iq_j}{\varepsilon_0\varepsilon_r r_{ij}} \quad (2)$$

where ε_{ij} is the energy parameter; σ_{ij} is the length parameter; r_{ij} is the distance between interacting atoms *i* and *j* measured from the centre of the particles; ε_0 is the dielectric permittivity of vacuum and ε_r is the relative permittivity, *C* is an energy-conversion constant, and q is the charge of atoms; *i* and *j* denote a pair of atoms. The cutoff distance is set to r_c = 10 Å. Lorentz-Berthelot combining rules are used for unlike-pair interactions, as shown in **eqn (3)** and **(4)**.[41]

$$\sigma_{ij} = (\sigma_{ii} + \sigma_{jj})/2 \quad (3)$$

$$\varepsilon_{ij} = \sqrt{\varepsilon_{ii}\varepsilon_{jj}} \quad (4)$$

The detailed Lennard-Jones and charge potential parameters for atoms of nitrogen and water molecules are shown in **Table 2**.

Table 2 Lennard-Jones and charge potential parameters of nitrogen and water molecules

Molecule	Atom	σ (Å)	ε (kcal/mol)	q (e)
Charged Nitrogen (gas)[34,35]	N	3.310	0.07154	-0.4820
	M (ghost atom)	-	-	+0.964
Water[36,37]	O	3.164	0.16275	-1.0484
	H	1	0	0.5242

2.2 Environment and configurations

To initialize the configurations with different volume fractions (ϕ), we defined a buffer size (BS): the distance between the edge of a single BNB to the edge of the cubic simulation unit, which is shown in **Fig. 1**. The initial configuration of this single nanobubble in water is created using PACKMOL.[42] The BNB has a radius of 2 nm centred in the middle of the simulation box. The initial density of the nitrogen nanobubble is set at 300 $\mathrm{kg/m^3}$ which is estimated from the expected density at a pressure expected for the nanobubble of 2 nm size using the Laplace equation. The density of the water was 996 $\mathrm{kg/m^3}$, commensurate with the expected density at 300 K for water. The volume fraction is defined by **eqn (5)** and is controlled by setting the buffer size. We replicated this simulation box with three units at the top and another three at the bottom, forming a larger cuboid simulation box (**Fig. 1 (b)**) containing 6 nanobubbles distributed evenly in the box. The periodic boundary conditions are applied in all three directions. By changing BS, ten different initial volume fractions ranging from ϕ_i=6.74%-28.10% have been examined in this research, as shown in **Table 3**. Following this, LAMMPS[43] is used for the subsequent simulations. Specifically, this 6 nanobubbles-water system for all volume fractions is equilibrated for 1 ns under the constant number of atoms, volume, and temperature (*NVT*) condition. This system is then equilibrated further for 2 ns under constant number of atoms, pressure (1 atm), and temperature (300 K) *NPT* conditions, which brings the system as close to its natural condition as possible at room temperature and pressure. In all simulations, a Nosé-Hoover barostat and thermostat are used to control the pressure and temperature, respectively. For this barostat, a damping constant of 2 ps is used. The thermostat uses a damping constant of 0.2 ps. The size of the simulation box and nanobubble changes slightly after equilibration under *NPT*, resulting in a slight variation in the final volume fractions listed in **Table 3**. Lastly, the Green-Kubo (GK) method is applied under the *NVT* ensemble for another 60 ns.

$$\phi = \frac{Volume\ of\ BNBs \times 100}{Volume\ of\ Simulation\ Box\ (including\ water\ and\ BNBs)} \quad (5)$$

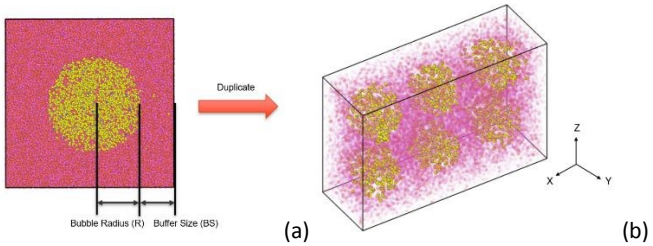

Fig. 1 The initial configuration for (a) a single 2nm nanobubble, the volume fraction is controlled by changing BS (b) six BNBs, water molecules are transparent red for clarity.

Table 3 Buffer size (BS), initial volume fraction (ϕ_i), number of nitrogen molecules (N_{N_2}), number of water molecules (N_{H_2O}), initial simulation box size ($X \times Y \times Z$) and final volume fraction (ϕ) for ten different volume fraction simulations. The cases in grey result in nanobubble coalescence. The remaining cases are used for GK simulations. The initial volume fraction under *NVT* and the final volume fraction after equilibration under *NPT* are given.

BS (Å)	ϕ_i	N_{N_2}	N_{H_2O}	$X \times Y \times Z$ (Å)	ϕ
4	28.10%	1296	15408	146×50×98	-
5	24.94%	1296	18294	152×52×102	-
6	22.23%	1296	21414	158×54×106	-
7	19.90%	1296	24780	164×56×110	-
9	16.14%	1296	32310	176×60×118	15.48%
11	13.26%	1296	40950	188×64×126	12.47%
13	11.03%	1296	50784	200×68×134	10.28%
15	9.28%	1296	61884	212×72×142	8.58%
17	7.87%	1296	74322	224×76×150	7.22%
19	6.74%	1296	88188	236×80×158	6.13%

2.3 Calculation of zero-shear viscosity

The zero-shear viscosity is calculated via the Green-Kubo (GK) method based on the fluctuation-dissipation theorem.[44,45] To be more specific, based on equilibrium fluctuations of the internal properties, the transport coefficients, such as thermal conductivity and viscosity, can be determined. This method relates the ensemble average of the auto-correlation function of stress to viscosity, according to linear response theory, which is one of the most common approaches for obtaining zero-shear viscosity in the computational molecular rheology field. The GK zero-shear viscosity (η) is governed by the **eqn (6).**[46]

$$\eta_{\alpha\beta}(t) = -\frac{V}{k_B T}\int_0^t [\sigma_{\alpha\beta}(0)\sigma_{\alpha\beta}(t')]dt' \quad (6)$$

where α and β refer to the Cartesian coordinates (x, y, z); t is the time; V is the total volume of the entire system; k_B is the Boltzmann constant; T is the temperature; $\sigma_{\alpha\beta}$ is the $\alpha\beta$ component of the stress tensor. η_{xy}, η_{yz} and η_{xz} are viscosity components obtained based on the ensemble average of the stress tensor σ_{xy}, σ_{yz} and σ_{xz}, by the given system volume, temperature and Boltzmann constant. Then, the GK zero-shear viscosity is the average of these viscosity components. It should be highlighted that the Irving-Kirkwood formalism is applied to calculate the stress tensor **σ** shown in **eqn (7)**.[47]

$$\sigma_{\alpha\beta} = -\frac{1}{V} < \sum_i^N m_i u_{i\alpha} u_{i\beta} + \sum_i^N \sum_{j>i}^N r_{ij\alpha} F_{ij\beta} > \quad (7)$$

where m_i is the atom *i* mass; $u_{i\alpha}$ *and* $u_{i\beta}$ are α and β components of the peculiar velocity of atom *i* because of the thermal fluctuations; $r_{ij\alpha}$ is the α component of the distance vector between atoms *i* and *j*; $F_{ij\beta}$ is the β component of the pairwise force vector between atoms *i* and *j*.

2.4 Calculation of shear viscosity

Couette flow was generated using the so-called NEMD SLLOD algorithm method. A constant shear rate was applied to the nanobubble systems generated and equilibrated at the earlier stages under *NVT* conditions. The atomic motion is governed by the **eqn (8).**[48]

$$\dot{\mathbf{r}}_i = \frac{\mathbf{p_i}}{m_i} + \mathbf{e_x}\dot{\gamma} r_{zi} \quad (8)$$

$$\dot{\mathbf{p}}_i = \mathbf{F}_i - \mathbf{e_x} p_{zi}\dot{\gamma} - \zeta \mathbf{p_i}$$

Where **r** is the position, **p** is the peculiar momenta, $\mathbf{e_x}$ is the unit vector in the flow direction (X direction); ***F*** is the force; *m* is the mass; *i* refers to the atom *i*; $\dot{\gamma}$ is the shear rate; ζ is the Nosé-Hoover thermostat. A Couette flow is generated through the SLLOD algorithm using the Lees-Edwards sliding bricks periodic boundary condition.[49] In this case, a linear velocity profile is generated across the Z dimension.[48] Therefore, $\dot{\gamma}$ is governed by the **eqn (9)**.

$$\dot{\gamma} = \frac{2U_x}{h} \quad (9)$$

where U_x is the velocity applied at the top edge of the simulation box in the shear direction; *h* is the size of the simulation box in the Z direction. The shear viscosity can be calculated via the **eqn (10)**.

$$\eta(t) = -\frac{\sigma_{xz}(t)}{\dot{\gamma}} \quad (10)$$

where σ_{xz} is the shear stress in the XZ plane. This method provides a comprehensive understanding of rheological behaviour for both non-Newtonian and Newtonian fluids.

2.5 Experimental setup

The Piping and Instrumentation Diagram (PID) of the nanobubble generation system is shown in **Fig. 2**. The experiment uses Trident™ Nanobubble System – 1 (TNS-1) as a bulk nanobubble generator. It consists of a tube, ejector nozzle (4 GPM / 1 m³/h) and a gas flow rate control valve from Trident Bubble Technologies LLC. A Rijing JLM60-B400A Automatic Self-priming Hot and Cold Water Pressure Pump with Flow Control pumps the water from the water tank. Milli-Q water is used to avoid contamination of the solution as much as possible. Ball valves #1 and #2 are located at the inlet and outlet of the pump, respectively, to control the water flow rate, which can also control the efficiency of the pump. The gas cylinder is connected to the Trident BNB generator. The gas flow rate can be directly controlled by the Trident BNB generator, which has been directly integrated into the generator by the manufacturer. The gas and water are mixed in the generator, producing the BNBs. The ball valve #3 at the generator's outlet controls the back pressure of the nozzle. This is a closed BNB generation system, and we ran at least four passes to get the BNBs.

The shear viscosity is measured by the Modular Compact Rheometer MCR302 from Anton Paar with the $\emptyset 26.65$ mm bob-cup measurement system. An Ostwald Viscometer can approximate the zero-shear viscosity of BNB-water solutions with a low capillary number. This assumes the fluid is Newtonian at low *Re,* as is the case for laminar flow experienced by fluid flow through a capillary. The size of the BNBs generated by this system is measured using a Zetasizer™ Nano ZS from Malvern and a ZetaView™ Quatt from Particle Metrix. The concentration (numbers per millilitre) of BNBs is measured by ZetaView™ Quatt from Particle Metrix.

To validate our measurements and compare them with our theoretical predictions, we also employed alternative approaches to measuring the concentration of nanobubbles and the volume fraction using a mass-based method. We used a 25 ± 0.03 mL beaker to measure the mass difference between pure Milli-Q water (pure water) and the BNBs-water solution with the same volume and then calculated the concentration and volume fraction of BNBs using the size measured by the ZetaView™ Quatt.

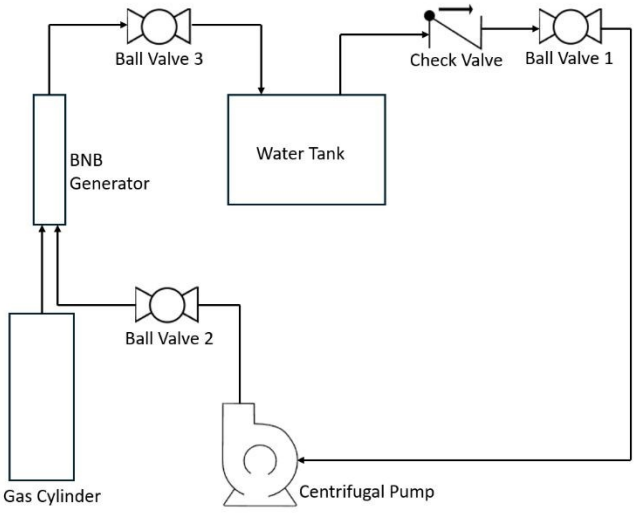

Fig. 2 PID of the nanobubble generation system

View Article Online
DOI: 10.1039/D5NR03076H

3 Results and discussions

3.1 Final-state BNBs-water system

For all simulations, we begin with a 1 ns *NVT* ensemble, followed by a 2 ns *NPT* simulation under standard conditions (300 K and 1 atm) to equilibrate the system. Following the equilibration phase, the nanobubbles shrink to slightly smaller sizes while part of the nitrogen atoms dissolve into water, and the simulation box size also shrinks slightly under *NPT* conditions. We have used OVITO's cluster analysis function to determine the average size of nanobubbles in the system after equilibration. The equilibrated volume fraction of nanobubbles for each system is then calculated and shown in **Table 3**. The resulting configuration is then used to calculate the zero-shear viscosity by simulating *NVT* conditions for 60 ns.

Our initial runs found nanobubbles coalesce when the buffer size is 7 Å or smaller ($\phi_I \geq 19.902\%$). In such cases, we will not calculate the viscosity due to the change in volume fraction. In recent work, Gao *et al*. have identified a charged double layer at the interface of BNB, with negative charges forming outside and positive charges inside the nanobubble.[12] Although multiple BNBs should all have a negatively charged interface leading to a repulsive force, they merge. This may be because the BS is too small, where the surface tension is not high enough to keep the nanobubbles stable.

The snapshot shown in **Fig. 3** illustrates the coalescence of two nanobubbles when the BS is 7 Å, after 30 ns of simulation. To observe BNB behaviour, we have hidden all the water molecules in the snapshot. The smaller buffer size cases are similar to the snapshot shown and will not be considered in this paper. This limits us to the simulation of systems with initial volume fractions of ϕ_I=6.71%-16.14% for calculating zero-shear viscosity.

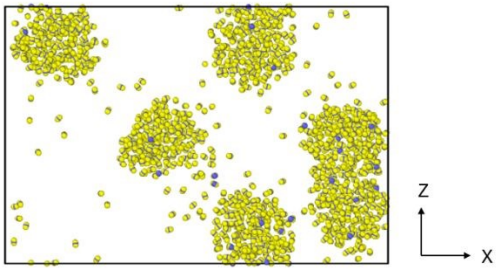

Fig. 3 The coalescence of nanobubbles when BS is 7 Å (ϕ_I =19.90%) after 30 ns. Water molecules are not shown for clarity.

3.2 Equilibrated density of BNB-water systems and size of nanobubbles

For 9 Å<BS<19 Å, the initial and equilibrated final-state volume fraction is shown in **Table 3**. Once the system is equilibrated, some nitrogen atoms dissolve in water, and the rest form stable nanobubbles. The overall density of the system depends on the volume fraction of the components. **Fig. 4** shows the density of the BNBs-water system versus the final BNB volume fraction. As shown in **Fig. 4**, with the increase of the ϕ, the density of the BNB-water system decreases due to the increase of the BNB volume and the decrease of the water volume. The final-state BNB average radius does not change significantly with the volume fraction and, on average, is *R*~19 Å, with an estimated internal gas density of ~330 kg/m³.

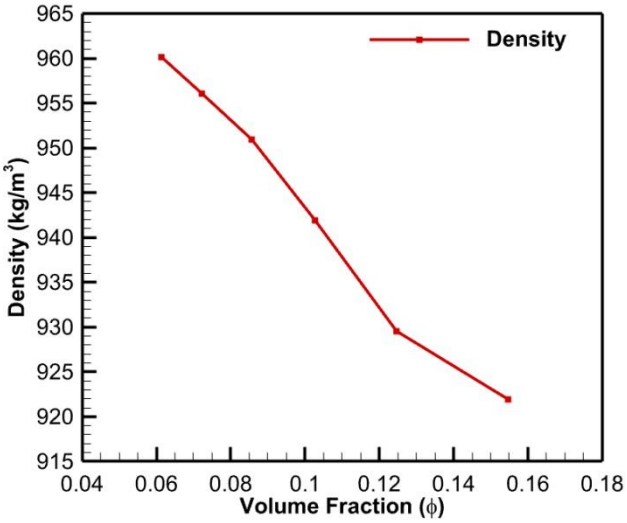

Fig. 4 Density of water-BNB system radius versus volume fraction.

3.3 Effect of volume fraction on gas solubility in water

We calculated the gas solubility of the BNBs-water system for each stable case by determining the number of dissolved N_2 molecules outside the nanobubble clusters. We used OVITO's cluster analysis to count the number of gas molecules dissolved in the surrounding water region after equilibrium, and we determined the solubility of BNBs at different volume fractions. As shown in **Fig. 5 (a)**, with the increase in ϕ (from 6.1% to 15.5%), the number of gas molecules dissolved into water increases, leading to increased solubility ranging from 0.58 to 1.5 g/L. We note that the solubility of N_2 in water under room conditions is 0.0014 g/L,[50] showing three orders of magnitude enhancement in the solubility of our nanobubble systems. The supersaturation ratio, *S*, is defined as the ratio of the calculated solubility of nitrogen in water for the BNB system to that under room conditions. **Fig. 5 (a)** shows supersaturation ratio as a function of volume fraction, which increases from 414 to 1074. A supersaturation ratio of approximately ~4 has been reported[51] in experiments for larger nanobubble (~200 nm) systems at lower concentrations. Our results show that this is significantly enhanced for smaller nanobubbles and higher concentrations.

3.3.1 Effect of supersaturation on the viscosity of water matrix

The significant increase in solubility of a gas in water raises a question about how this dissolved gas affects the viscosity of water. There is a lack of research on the effect of dissolved gas on this highly supersaturated state of water.

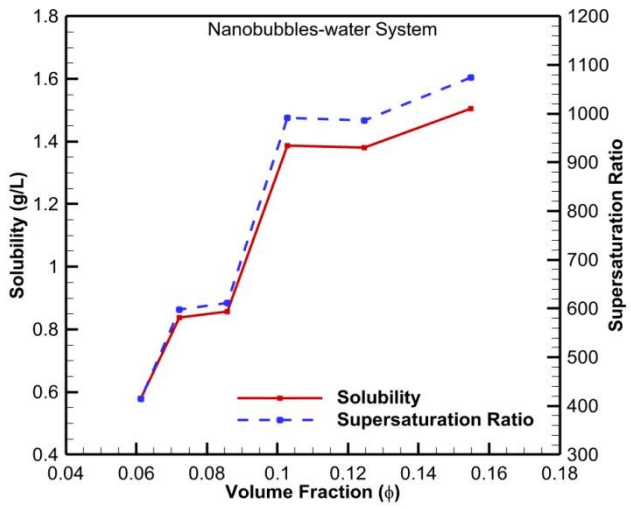

(a)

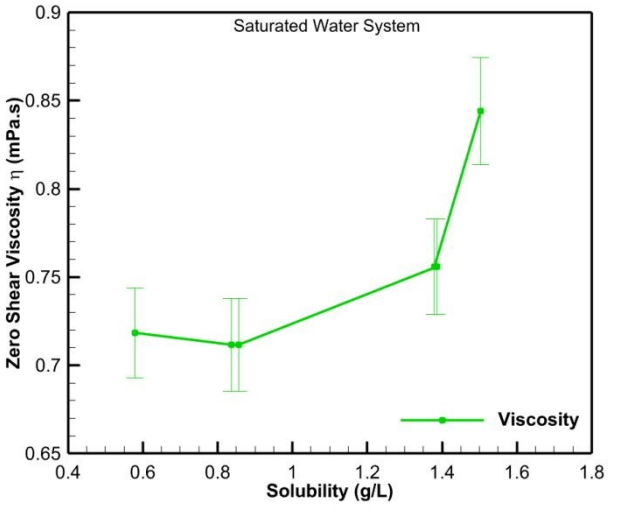

(b)

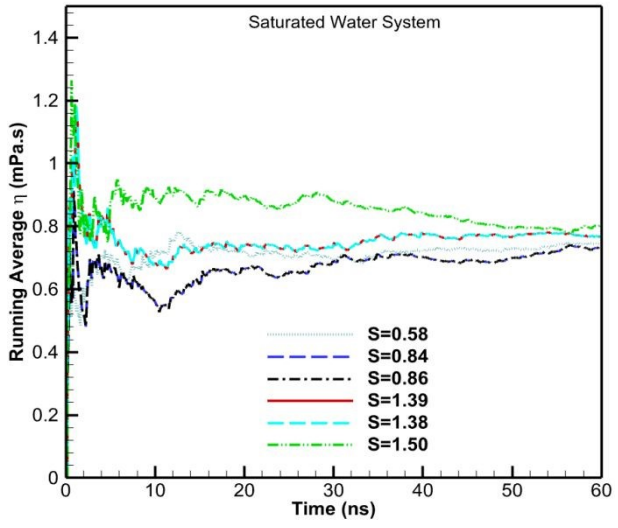

(c)

Fig. 5 (a) Solubility (solid line) and supersaturation ratio (dashed line) versus volume fraction for the BNBs-water systems, (b) the zero-shear viscosity versus solubility for the saturated water systems, and (c) running average zero-shear viscosity versus time for various systems with different supersaturation ratios.

To the best of our knowledge, no previous studies in the literature have investigated this effect; therefore, we conducted our own simulations to explore this phenomenon. We created supersaturated N_2-water systems (without BNBs) with identical solubility as the BNBs-water systems at corresponding ϕ (**Fig. 5 (a)**).

We repeated the same procedures for preparing and equilibrating these systems; however, in the initial phase, N_2 molecules were randomly dispersed in water to create a dissolved gas model. Equilibrium simulations were conducted for 1 ns under *NVT*, followed by 2 ns under *NPT*. Finally, a 60 ns *NVT* simulation was conducted to obtain the GK zero-shear viscosity. **Fig. 5 (c)** shows that these saturated water systems' viscosity is stabilized after 60 ns. The final average zero shear viscosity is plotted in **Fig. 5 (b)** versus solubility. The running sum method is used to calculate statistical errors from the block-averaged values of the zero-shear viscosity every 0.1 ns. More details on error analysis are available in the Supplementary Information (SI). We can see that an increase in the solubility results in only a slight change in the water matrix viscosity, which is statistically significant only at the highest volume fraction of 15.5%. Therefore, these dissolved gas molecules in water can only be a factor affecting the rheological behaviour of our BNBs-water system at high volume fractions, which will be discussed in the following session.

3.4 Zero shear viscosity for BNBs-water system

We have also calculated the GK zero-shear viscosity of the BNBs-water system. **Fig. 6**. shows the running average of zero-shear viscosity from the GK method plotted against time for 60 ns of the simulation duration. The results indicate that the systems are fully equilibrated and have reached a steady state.

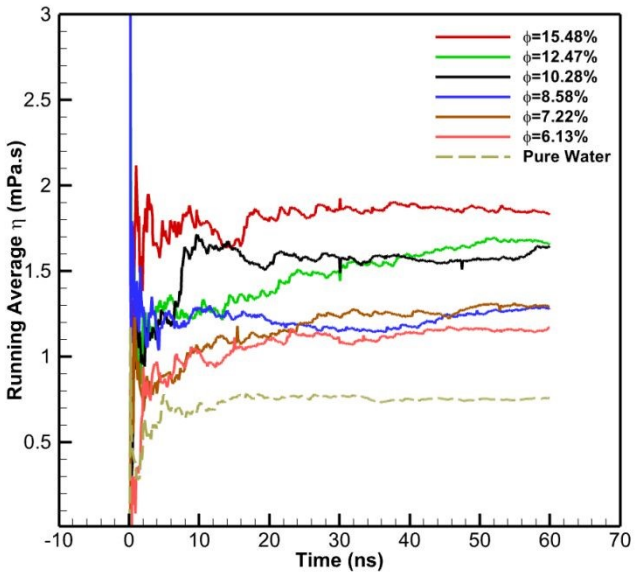

Fig. 6 Zero-shear viscosity versus time obtained from MD-GK simulations for BNBs-water systems of different volume fractions. The result for pure water is also shown (dashed line).

We have also simulated pure water using the TIP4P(Ewald) model, resulting in a zero-shear viscosity (η_w) of 0.76 ± 0.02 mPa.s, which is within 10% of the experimental value of 0.85 mPa.s reported[52] for water at 300K. We are unaware of other GK simulations of TIP4P(Ewald) reporting water viscosity at 300 K. However, Markesteijn *et al.*[53] have reported a close value of 0.705 mPa.s at 303 K using Poiseuille flow for the TIP4P(Ewald) model. We note that the viscosity of the supersaturated water matrix (**Fig. 5 (b)**) exhibits a slight reduction compared to pure water at solubility values corresponding to lower volume fractions. However, for the highest solubility, corresponding to the highest volume fraction, the viscosity is higher than pure water. Nevertheless, the change in water matrix viscosity due to gas dissolution is small. Therefore, to follow the convention in studying suspensions, the relative viscosity is calculated based on the viscosity of pure water ($\eta_r = \eta_{BNB}/\eta_w$). **Fig. 7** shows the relative viscosity, which is the ratio of the GK zero-shear viscosity of the BNBs-water system for that volume fraction and the corresponding GK zero-shear viscosity of the pure water. The running-sum method is used to calculate error bars based on the block-average of the zero-shear viscosity every 0.1 ns, as detailed in the SI.

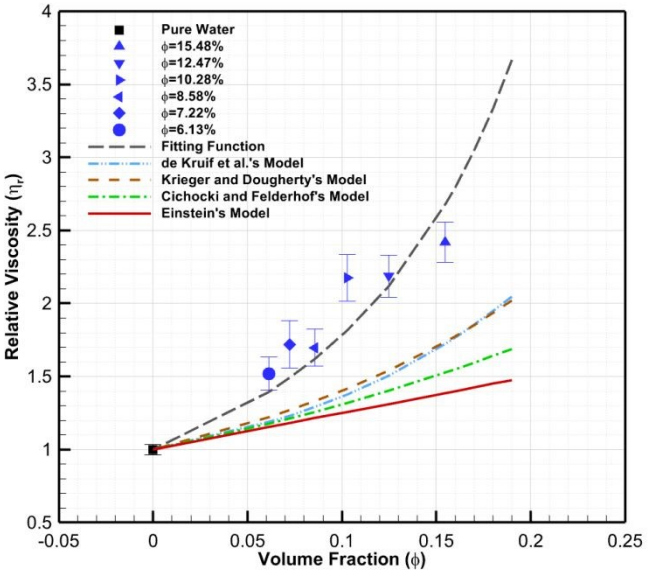

Fig. 7 Relative viscosity (η_r) versus volume fraction (ϕ). The results are shown from our molecular dynamics (MD) simulations (symbols) and several suspension rheology models (lines). The dark dashed line is the fitting to the MD results (**eqn (17)**).

In **Fig. 7**, we have also plotted the relative viscosity versus volume fraction for several theoretical models for colloids and suspensions. The solid red line refers to the classic Einstein's model for a dilute suspension of spheres governed by **eqn (11)**.[54]

$$\eta_r = 1 + \frac{5}{2}\phi \quad (11)$$

Taylor's seminal work[55] generalized Einstein's equation for suspensions of fluid droplets in another liquid, given by **eqn (12)**, where $[\eta]=(5\lambda+2)/2(\lambda+1)$, is the intrinsic viscosity, and $\lambda=\eta_p/\eta_s$ viscosity ratio of dispersed and suspending fluids. Note that for rigid particles $\lambda\to\infty$, we recover $[\eta]$=2.5 from Einstein's equation. For air bubbles, one expects $\lambda\to 0$, and we obtain $[\eta]$~1.

$$\eta_r = 1 + [\eta]\phi \quad (12)$$

The Krieger-Dougherty model (brown dashed line) is governed by **eqn (13)**.[56]

$$\eta_r = \left(1 - \frac{\phi}{\phi_m}\right)^{-[\eta]\phi_m} \quad (13)$$

where ϕ_{m} is the maximum packing fraction, and $[\eta]$ is the intrinsic viscosity. $[\eta]$ can also be obtained from the slope, $d(\eta_r)/d(\phi)$, of viscosity versus volume fraction in the low volume fraction region, which has a linear behaviour. When the shear rate is close to 0, the ϕ_{m} is set to 0.63, which refers to the ϕ of the random close packing of hard spheres,[57,58] and the $[\eta]\phi_m$ is set to 1.96.[57] Then, the **eqn (13)** will become **eqn (14)**.

$$\eta_r = \left(1 - \frac{\phi}{0.63}\right)^{-1.96} \quad (14)$$

The de Kruif *et al.*'s model (blue dash-dot-dot line) for hard-sphere colloidal dispersions when the shear rate is close to 0, given by **eqn (15)**. [57]

$$\eta_r(\dot{\gamma}\to 0) = 1 + \frac{5}{2}\phi + 6\phi^2 + 52\phi^3 \quad (15)$$

The green dash-dot line represents Cichocki and Felderhof's model for dilute suspensions of spherical Brownian particles, governed by **eqn (16)**.[59]

$$\eta_r = 1 + \frac{5}{2}\phi + 5.91\phi^2 \quad (16)$$

It is interesting to notice that all these models underestimate the zero-hear viscosity of the BNBs-water system. However, the Krieger-Dougherty model is the closest. Therefore, we have fitted our MD data to the Krieger-Dougherty model (**eqn (13)**). By using ϕ_{m}, as a fitting parameter we obtain ϕ_{m}=0.39 and $[\eta] = 5.0$. Therefore, the fitting function based on the BNBs-water system is governed by **eqn (17)**. The reduced maximum packing fraction ϕ_{m}, indicates that due to repulsive forces between nanobubbles the effective diameter of the nanobubbles is larger, leading to a reduced jamming volume fraction.

$$\eta_r = \left(1 - \frac{\phi}{0.392}\right)^{-1.96} \quad (17)$$

The plot demonstrates that as the volume fraction (ϕ) increases, the zero-shear viscosity rises correspondingly. Notably, the zero-shear viscosity of these highly concentrated small bulk nanobubbles (BNBs) is significantly higher than that of pure water. This behaviour contrasts with what is typically observed in macro-bubble water systems and nanobubbles made from cavities.[23] Moreover, the relative viscosities of BNBs obtained from molecular dynamics (MD)

simulations exceed the predictions of classical theoretical models for dilute hard-sphere colloidal dispersions, highlighting the unique rheological behaviour of these nanoscale systems. The colloidal behaviour of these nanobubbles persists throughout the simulation time and can be observed from the snapshots shown in **Fig. 8**, illustrating the dynamic behaviour of these six BNB-water systems over 60 ns. The snapshots show that all 6 BNBs are stable and randomly and evenly distributed in the simulation box during the entire 60 ns of simulation time, similar to colloidal dispersion behaviour. For micro-bubbles of 0.24-0.29 mm size suspended in corn syrup, Rust and Manga[18] have reported increased viscosity with volume fraction at low capillary numbers, which is a ratio of viscous to capillary forces $Ca=R\dot{\gamma}\eta/\Gamma$ (R is bubble radius, η is the solvent viscosity, $\dot{\gamma}$ refers to the shear rate, and Γ is the surface tension).

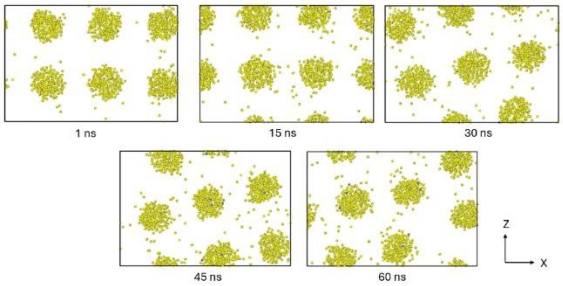

Fig. 8 The snapshot of the behaviour of BNBs with time for ϕ=12.5% case, showing no coalescence. (water molecules are not shown)

However, their results fit well with the Krieger-Dougherty model, with $[\eta]\sim 1\ and\ \phi_{\mathrm{m}} = 0.6$, consistent with the expectation for bubbles. Unusually large $[\eta]\sim 13.5$ is reported[19] for bubbles in molten Germania, albeit at much larger capillary numbers Ca>>1. The reported viscosity of nitrogen at T=300 K and ρ=330 kg/m^3 is 0.029 mPa.s.[60] Therefore, viscosity ratio of λ=0.029/0.76=0.038, leading to $[\eta]$=1.06, which is significantly smaller than 5.0, the value we obtained from the fitting. This deviation, while surprising, can be explained by charge effects. Studies on charged silica nanoparticle (R~10 nm)[61] suspensions in water have shown significant deviation from the Krieger-Dougherty model for hard spheres, leading to $[\eta]$ =4.74 for particles with zeta potential of ζ=-66.35 mV. Nitrogen nanobubbles are charged with a zeta potential reported to be approximately -20 mV in the literature.[62] The formation of a nanobubble's negative surface charge is attributed to the preferential orientation of water molecules at the interface, resulting in an electrical double layer (EDL). The negatively charged oxygen atoms concentrate at the outer layer of the EDL, while the positively charged hydrogen atoms form the inner layer. This interfacial structure leads to a net negative potential at the bubble surface, despite the absence of free ions or net molecular charge, and is consistent with experimental observations of nanobubbles exhibiting negative zeta potentials. Similar behaviour has been reported by Gao *et al.* [12], who observed EDL formation and water molecule orientation around ~2nm oxygen nanobubbles using all-atom molecular dynamics simulations. The zeta potential can be determined if either the surface charge density or the surface potential is known. We have used the charge density to calculate the ζ-potential of the R=1.9 nm BNB used in this research and of a larger nanobubble (R=4.27 nm), almost twice the size. The ζ-potential is ~-3.14 mV and ~ -4.85 mV, respectively (more details can be found in SI). However, the calculated ζ-potential (~-3.14 mV and ~ -4.85 mV) of these BNBs is smaller than the ζ-potential (~-20mV) in magnitude measured from the experiment with a radius around a few hundred manometers. This is because BNB's smaller size results in a lower charge density.

There is a striking similarity between the rheological behaviour of the nanobubbles we obtained here and that of charged nano-silica particles, which points to the charge effects in the observed behaviour. Despite the absence of free ions or dissociated species in our simulations and experiments conducted in pure water, the observed negative zeta potential can be attributed to the preferential orientation of interfacial water dipoles at the gas–liquid interface. Our molecular dynamics simulations (See SI) show that water molecules form a structured dipolar layer. This collective dipole arrangement generates a measurable electrostatic potential at the nanobubble surface even in the absence of net charge. Consequently, nanobubbles can exhibit electrostatic repulsion analogous to that of charged colloids (with free charges), driven by interfacial polarization rather than free surface charge.

It should be noted that the fitting model (**eqn (17)**) presented here is developed for a monodisperse system of BNBs with uniform size and may need to be refined for polydisperse systems. In other words, in experiments, due to the polydisperse size distribution of BNBs and their larger sizes, our model may overestimate or underestimate the actual viscosity of the BNBs-water solution. We will attempt to test the accuracy of this model using experiments. However, it should also be noted that controlling the size of BNBs and their volume fraction is challenging with the current technology. However, we will do this for one volume fraction.

3.5 Effect of shear on the nanobubbles

The NEMD SLLOD algorithm is used to simulate the Couette flow. The shear rates range from $1\times10^{8}\,\mathrm{s}^{-1}$ to $1\times10^{10}\mathrm{s}^{-1}$ in the simulations. MD simulations are limited to high shear rates to obtain reliable and statistically relevant values for shear viscosity. However, due to the high shear rates, in most cases, the BNBs are unstable, which means ϕ changes with time. In those cases, the shear viscosity will not be calculated, and we will focus on the effect of shear on the stability of the nanobubbles. Here, we find three distinct behaviours for these unstable BNBs under these high shear rates:

(i) BNBs merge, forming a bigger bubble

We observe different behaviours depending on the volume fraction or the shear rates. Even at the lowest shear rates we examined, the bubbles merge into larger bubbles. The bubbles merge into bigger bubbles at high volume fractions and lower shear rates. In this case, we can observe the coalescence of multiple BNBs, similar to the case

shown in **Fig. 9 (a)** and **(b)**, where two nanobubbles merge, forming a bigger one and resulting in the change of the ϕ.

(ii) All BNBs merge, forming a cylindrical shape.

In this scenario, multiple BNBs coalesce, creating a cylindrical formation. Due to the periodic conditions of the simulation box, this cylindrical gas bubble indicates that the bubbles are merging with other BNBs in the neighbouring simulation boxes. To gain a clearer view of the cylindrical bubble, the water molecules are also depicted in **Fig. 9 (c)**.

(iii) BNBs dissolved into water

When ϕ is high, under shear flow all the gas molecules in the BNBs will dissolve into water. In this case, the nanobubbles merge entirely with the water. **Fig. 9 (d)** shows the case where BS=5 Å under 1×10^{10} s^{-1} where gas molecules in all six BNBs dissolved into water.

In the MD simulations, BNB coalescence under shear leads to system instability, with higher shear rates causing an earlier onset of instability. At the low shear rates of $3.3 \times 10^7, 5 \times 10^7, 10^8$ s^{-1}. We successfully measured the NEMD SLLOD shear viscosity of the BNB-water system at four volume fractions before coalescence. The running average of shear viscosity at this rate, calculated over a simulation time of 5-20 ns, depending on the system, is obtained before coalescence. Details of the simulation time are reported in the SI. The running-sum method is used to calculate error bars based on the block-averaged shear viscosity values every 0.1 ns; details are provided in the SI. At higher shear rates, viscosity was not calculated due to insufficient statistical reliability, as coalescence occurred within ~0.1 ns.

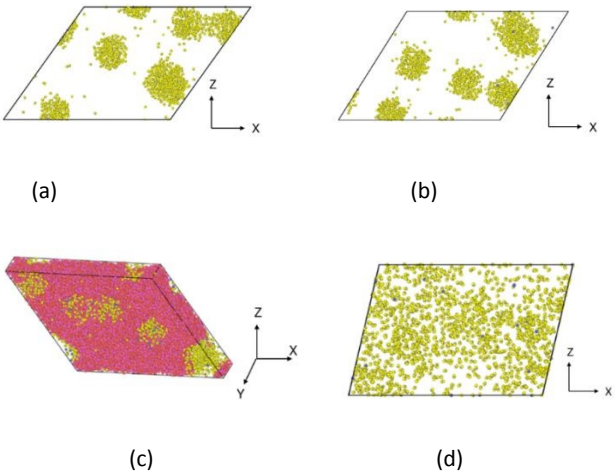

Fig. 9 Coalescence of two BNBs can be observed for ϕ=15.5% at the lowest shear rates of (a) 1×10^8 s^{-1}, and (b) 3.262×10^8 s^{-1}; (c) Cylindrical gas bubble for the case BS=9 Å and 1×10^8 s^{-1}; (d) All gas molecules dissolved into water for a high volume fraction of 25% under a 10^{10} s^{-1} shear rate.

The results in **Fig. 10** show that as the volume fraction increases, the shear viscosity increases, a trend also observed for zero-shear viscosity. The corresponding zero shear viscosity values at these volume fractions are shown with arrows in this figure. This shows that the shear viscosity has increased up to a shear rate of 5×10^7 s^{-1} for all volume fractions. This indicates a possible shear-thickening effect before the coalescence. This shear thickening happens at a surprisingly lower volume fraction than those reported for hard spheres (ϕ > 30-40%)[63]. Also, this shear thickening appears transitory, as seen by the destruction of nanobubbles at higher shear rates. Due to this effect, it is impossible to determine the onset shear rate for the shear thickening effect, which might be much lower than those accessible to MD simulations. By contrast, with further increase of the shear rate from 5×10^7 s^{-1} to 10^8 s^{-1}. We observe a shear-thinning effect with decreasing shear viscosity. The onset of shear thinning for the ϕ=12.47% is not clear, and it may occur at lower shear rates. This is consistent with the general behaviour of colloid suspensions, where the onset shear rate of shear thinning decreases with increasing volume fraction[64].

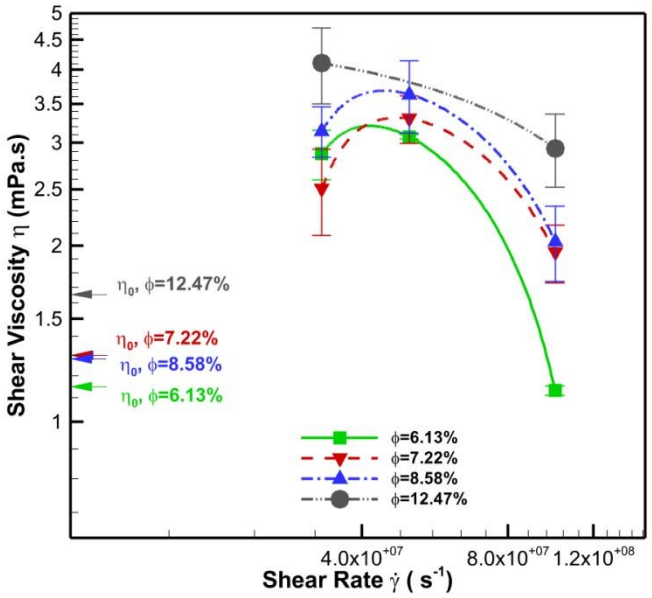

Fig. 10 The shear viscosity versus shear rate between $3.3 \times 10^7 - 10^8$ s^{-1} (in log-log format) for different volume fractions. The arrows show the zero-shear viscosity for those volume fractions.

3.6 Experimental results

The experiment measured the shear viscosity of pure water (Milli-Q), nitrogen BNB, and air BNB water solution samples twice at T=25℃. The average results are shown in **Fig. 11,** where each line in the plot represents the average results of two samples. Firstly, the fresh BNB sample was put into the cup, and the shear viscosity was measured by gradually increasing the shear rate from 0 to 100 s^{-1}. These fresh BNB samples for nitrogen and air nanobubbles (red dashed and blue dash-dot-dotted lines in **Fig. 11**) exhibited a significantly higher viscosity than pure water at shear rates below 35 s^{-1}. At higher shear rates, the viscosity of BNB systems dropped to that of pure water. To test whether there would be a recovery after cessation of shear, with dissolved gas forming nanobubbles, we removed the bob, waited for a few minutes, and then reinserted it into the cup, measuring the shear viscosity again over the same range of shear rates. As shown in

Fig. 11, we tested both nitrogen and air BNBs-water solutions. The second measurement (black solid and green long-dash lines in **Fig. 11**) of the same sample provides robust evidence that there is no BNB in the solution where the sample's viscosity is precisely the same as that of pure water. This finding is consistent with our simulation results, which indicate that the presence of BNBs in water at a lower shear rate leads to higher viscosity. However, higher shear rates destroy the BNBs, reducing the solution viscosity to that of pure water. We used a ZetaSizer™ to measure nanobubble sizes, finding mean radii of ~251 nm for nitrogen and ~232 nm for air BNBs. Although the size of the BNBs in experiments is larger than the BNBs in the simulations, we still observed that the viscosity of the BNB-water solution is higher than that of pure water at low shear rates. However, the increased viscosity in the experiments at lower shear rates is more than that obtained from the simulations. We are not sure why we observe such a difference. In experiments with nanobubbles in water, we are limited to extremely low *Ca* numbers due to the water's low viscosity, low shear rate, and small bubbles. The capillary number for the experiments was very small, on the order of 10^{-7} to 10^{-9}. Therefore, one expects the nanobubbles to remain approximately spherical, leading to increased viscosity. However, the rapid decrease in viscosity with increasing shear rate, which leads to an irreversible decline in viscosity to that of water, suggests the possible coalescence of nanobubbles and their eventual release into the environment.

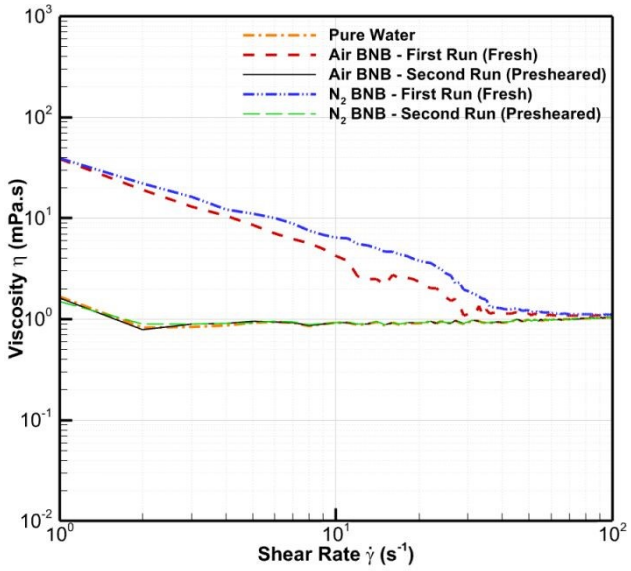

Fig. 11 Experimental shear viscosity versus shear rates in log-log scale for pure water (orange dash-dot line), air (red and black lines) and nitrogen (blue and green lines) BNBs-water solutions. The results for the fresh BNB and presheared samples have been shown separately. The average nanobubble radius is *R*~232-251 nm.

There could be some contribution to the increased viscosity due to the formation of surface nanobubbles on the surface of the rheometer probe. There are also different time and length scales in the experiments. The shear simulations capture only a few nanoseconds of the simulation and are possible at longer time scales; coalescences result in the destruction of nanobubbles and a reduction in viscosity, similar to experimental observations. It is essential to note that achieving BNB sizes of just a few nanometres, as used in the simulation, and maintaining precise control over their size and volume fraction remain significant challenges in the field. It should be noted that these exploratory, experimental results provide qualitative behaviour consistent with simulations. However, these should be investigated and refined. Therefore, we also produced new samples of nitrogen nanobubbles with reduced diameters. We successfully reduced the nanobubble size to ~70 nm and repeated the shear sweep measurements using the rheometer. The viscosity of these BNBs was measured using both a rheometer and a traditional Ostwald viscometer. To compare the results with those measured by the Ostwald viscometer, the temperature of these measurements is controlled at room temperature on that specific day (T = 22°C). The average viscosity versus shear rate for both the fresh and presheared samples is plotted in **Fig. 12 (a)**.

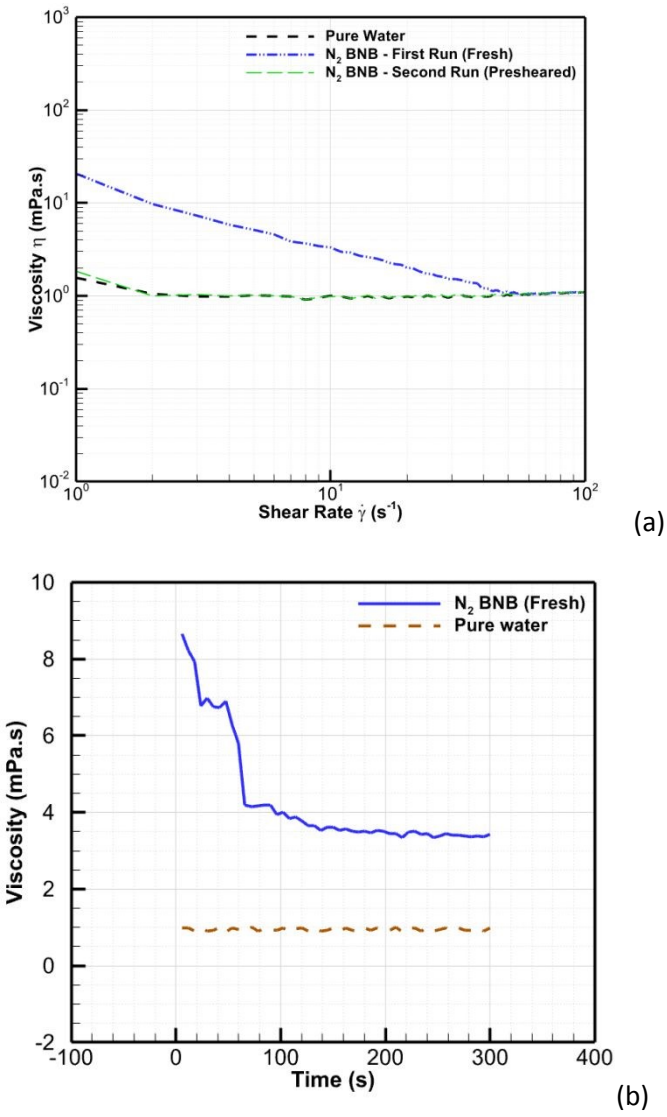

Fig. 12 Viscosity of nitrogen BNBs-water solution and pure water (a) versus shear rate in log-log scale and (b) under constant shear rate (5 s^{-1}) at 22°C. The average nanobubble size is *R*~70 nm

Each line in the plot is the average of two measurements. The trend observed was similar to larger nanobubbles in **Fig. 11**. However, the initial viscosity seems to be about half of the initial viscosity of these larger nanobubble samples. This may be because those larger bubbles are more likely to form surface bubbles, leading to a higher initial viscosity. We also measured the shear viscosity under a constant shear rate of 5 s^{-1} for 5 minutes using a rheometer. We have taken measurements for three fresh BNBs-water samples with the same BNBs generation settings, as well as for pure water. The average results are shown in **Fig. 12 (b)**, which clearly demonstrates that the steady-state viscosity of the BNBs-water solution (3.44±0.00018 mPa.s) is higher than that of pure water (0.95±0.0030 mPa.s). The measured viscosity of pure water is only ~0.88% different from the literature data (0.9544 mPa·s).[65] The same reason that increasing shear rates can explain the initial drops in the BNBs-water solution can also explain the initial drops in the BNBs-water solution. However, it was evident that, after ~2 minutes, the viscosity of BNBs-water solutions became stable, and the steady-state viscosity of the BNBs-water solution was much higher than that of pure water, even higher than that predicted by our fitting model. This may be because, under a constant low shear rate, surface bubbles and microbubbles are unlikely to be destroyed, resulting in an unexpectedly high viscosity and Newtonian behaviour. Thus, we believe there is a critical shear rate that will lead to the disappearance of BNBs and a significant decrease in viscosity, which may depend on bubble size, volume fraction, and surface interactions. Comparing **Fig. 12 (a)** and **Fig. 11** suggests the critical shear rate is slightly higher (~45 s^{-1}) for the smaller bubbles of ~70 nm than that of 35 s^{-1} observed for larger 251 nm bubbles. Further research will be necessary in the future to fully understand this phenomenon. In the next section, we will use an Ostwald viscometer to compare our results with those obtained here. Determining the Concentration and Volume Fraction of Nanobubbles

To validate the experimental results and compare them with the model we developed from the simulation, we need to determine the volume fraction in our BNB system produced by the experiments. To achieve this, we require the concentration of nanobubbles and their corresponding size. Here, we determined the concentration using a ZetaView™ machine and also measured the mass of the gas in BNB systems. We will see how they compare.

3.6.1 Concentration from ZetaView (N_{ZV})

We measured concentration (N_{ZV}) and radius (R) of these nitrogen nanobubbles as $(5.63 \pm 0.83) \times 10^8$ particles per mL and 70.584 ± 2.08 nm using a ZetaView™ Quatt machine at 22℃. The concentration of nanobubbles is very close to the upper limit mentioned by the manufacturer (10^9 particles per mL)[66]. Therefore, we will use a secondary method to confirm this. We will see how this compares with the concentration from the mass of the gas.

3.6.2 Concentration from mass analysis (N_m)

View Article Online
DOI: 10.1039/D5NR03035H

We can determine the number density of BNBs by measuring the mass and volume of the gas in the BNB solution. We measured these properties three times to reduce the errors. To achieve this, we must determine the mass and densities of pure water and BNB solutions. We used a beaker with a volume of V_b=25 mL to determine the densities by weighing the mass of pure water (m_1), and BNBs-water solution (m_2) at 22℃. We determined the density of BNBs solution as ρ_{BNB}=992.78 ± 0.30 kg/m^3 and pure water as ρ_w=994.14 ± 0.21 kg/m^3, which is within 0.37% of the literature data at 22℃ (997.8 kg/m^3)[65]. As expected, the density of BNBs-water solution is smaller than the density of pure water because of the lower density of BNBs compared to water. This approach is similar to that taken by Ohgaki *et al.*[32]. We will also need these density values to determine the viscosity using the Ostwald viscometer.

The internal pressure of the N_2 nanobubble is approximately 2 MPa, estimated from the Laplace equation $P = 2\Gamma/R$, where R is the average radius of the BNB (70.584 nm), and Γ is the liquid's surface tension (71.1 mN/m)[67]. The corresponding density of N_2 (ρ_{N_2}) under 2MPa and 22℃ is 22.9 kg/m^3.[68] Following this, we can get the total volume of gas in the sample $V_g = \rho_{N_2}/(m_1 - m_2) = 1.49 \times 10^{-6}$ m^3. The calculated concentration (N_m) and volume fraction (ϕ) in this experiment can be obtained via **eqn (18)** and **(19)** respectively.

$$N_m = \frac{V_g}{\frac{4}{3}\pi R^3 \times V_b} = 4.032 \times 10^{13} \text{ BNBs per mL} \quad (18)$$

$$\phi = \frac{V_g}{V_b} \times 100 = 5.94\% \quad (19)$$

It is clear to see that the mass-based concentration N_m is far higher than N_{ZV} from the measurement using the ZetaView™ Quatt machine. This is four orders of magnitude higher than the upper limit of the ZetaView™ Quatt (10^9 particles per mL) [66]. Therefore, we believe that the concentration measured by the ZetaView™ Quatt is not accurate. Ohgaki *et al.*'s group[32] has reported a concentration of 1.9×10^{13} BNBs per mL for their 50 nm BNB solution, which is in the same order of magnitude as what we obtained, using a similar approach to calculate the concentration.

3.7 Viscosity from the Ostwald viscometer and comparison with the suspension model

The viscosities of pure water and BNBs-water solution at room temperature (T=22℃) are obtained as 0.93±0.0014 mPa.s and 1.17±0.00074 mPa.s, respectively, using an Ostwald viscometer measured three times, considering the density of the solution. The measured viscosity of pure water is within 2.2% of the literature data at 22℃ (0.9544 mPa·s)[65]. Therefore, we observe a 25.67% increase in the viscosity of the BNBs-water solution using this alternative method compared with pure water. However, the viscosity of the BNBs-water solution is lower than that measured by the rheometer. The surface area in the bob-cup rheometer is much larger than that in the capillary viscometer, and these factors may contribute to the

formation of surface nanobubbles. The Anton Paar bob-cup rheometer has a significantly larger surface area in contact with the fluid—~20 times greater than that of our Ostwald viscometer (D=1 mm, L=12.3 mm). This larger surface area can influence measurements, especially in systems where surface interactions (e.g., nanobubble adhesion) play a role. Furthermore, we calculate the average shear rate ($\dot{\gamma}_{avg} = \frac{16Q}{\pi D^3} = 184\ s^{-1}$) for the flow rate of Q, through our viscometer. The shear rate is significantly higher than the critical shear rate of ~45 s^{-1}, as observed with the rheometer, at which the viscosity drops to that of water. The persistently higher viscosity we measured using the Ostwald viscometer, with minimized surface effects, suggests that the viscosity obtained with the Ostwald viscometer is closest to the bulk viscosity of the BNB system. Therefore, we have used the viscosity from the Ostwald viscometer to compare the results with our model.

Using ϕ=5.94% and the measured viscosity of η_{0w} =0.93 mPa.s in our fitting model (**eqn (17)**), the viscosity of BNBs-water solution is calculated as $\eta_{0,BNB}$ =1.29 mPa.s. This is only 8.93% higher than the viscosity of 1.173 mPa s that we measured using the Ostwald viscometer. This agreement is particularly robust, considering the significant differences in bubble size distributions between the simulation and experimental setups. In our simulation, the BNBs are monodisperse—uniform in size—whereas the experimental data involve a polydisperse system with a range of bubble sizes. Our fitting model assumes a consistent BNB size, but in reality, larger bubbles tend to reduce the measured viscosity. As a result, the 8.93% higher viscosity observed in the simulation is a reasonable outcome, reflecting the expected impact of size variability in the experimental conditions.

4 Discussion and conclusion

In this research, we have studied the rheological behaviour of highly concentrated BNBs, focusing on the zero-shear viscosity, shear viscosity and the effect of volume fraction and flow on their stability. We refer to nanobubble concentrations in the range of 7–28% volume fraction as 'highly concentrated' in the context of nanobubble research, where reported values are typically much lower. While these concentrations may be considered moderate compared to colloidal suspensions or micellar systems, they are near the upper limit currently achievable for nanobubbles due to challenges in generating and stabilizing them. Our experimental system, reaching approximately 6%, represents one of the highest concentrations reported to date. Simulations extend this range to 6.1–15.5% to explore rheological behaviour under conditions that remain challenging to realize experimentally, offering insight into the behaviour of dense nanobubble suspensions.

We find that the zero shear viscosity of the BNB-water system is higher than that of pure water. Moreover, with the increase of the ϕ, the zero-shear viscosity increases. The results can be fitted to a modified Krieger-Dougherty model, indicating that when nanobubbles are evenly distributed in water, they behave like colloidal dispersions. At high volume fractions, the BNBs become unstable and coalesce. We have measured the gas solubility in the water matrix surrounding nanobubbles to be three orders of magnitude higher than that of solubility at room conditions. The supersaturation ratio increases with volume fraction. We demonstrate that the viscosity of this supersaturated water matrix is influenced by the dissolved gas content only at the highest concentration, and there is only a negligible effect on the viscosity of the BNB-water system. However, the primary increase in the viscosity is due to colloidal behaviour.

In the simulations, shear viscosity could not be calculated for a wide range of shear rates and volume fractions because the BNBs became unstable at high shear rates and volume fractions. They coalesce or completely dissolve in water, leading to the change of ϕ, so the shear viscosity cannot be calculated under different shear rates for most of the volume fractions considered here. The cause of the coalescence under shear rates is different from that under zero-shear conditions. However, we could calculate the shear viscosity at the lowest shear rate for four different volume fractions, which showed no coalescence. These systems exhibited viscosities higher than that of pure water and also higher than the corresponding zero-shear viscosity of the BNB system at the specified volume fraction. This behaviour suggests a short-lived transitory shear-thickening effect of these BNBs-water systems before coalescence occurs. The shear viscosity also increased with the increase in volume fraction.

The capillary number of Ca=2.3×10^{-3} is obtained for the shear rate we simulated and examined in this work using the R=1.9 nm η_w=0.76 mPa.s, Γ=61.7 mN/m[69] for TIP4P(Ewald) model. At this very low capillary number, one would expect the viscosity to be close to that obtained for zero-shear viscosity; however, it is higher. Therefore, we need further investigation by other means in the future to better understand the effect of shear rate on the results. One of the limitations of SLLOD is that it imposes a linear velocity profile across the simulated fluid, leading to the deformation of nanobubbles at the same rate as the surrounding fluid. The timescale of the simulations is also much smaller, and phenomena related to the coalescence and release of the nanobubble gas may require longer timescales to be observed in the simulation. While we see this in the experiments, the limitation of the simulation is that we may not observe the full behaviour. Other approaches, such as boundary-driven or Poiseuille flow, can be used to simulate these systems and gain a better understanding of a broader range of shear rates. Nevertheless, the simulations of zero-shear rate viscosity show that viscosity increases with volume fraction, in agreement with those reported for microbubbles in viscous fluids such as corn syrup and silicon oil.[18,20] However, the increase is higher than that reported for these microbubbles. We believe that the charged nature of the nanobubbles may contribute to the observed difference.

To validate the rheological model developed from the simulation, we produced nanobubbles with a radius of ~70 nm at the highest concentration reported to date (4.0 × 10^{13} BNBs/mL) in our laboratory and successfully determined their volume fraction. By

measuring the concentration of nanobubbles using a mass-based approach and an NTA machine, we demonstrated that the current NTA technology for measuring the concentration of BNBs may not be accurate for highly concentrated BNBs.

The discrepancy between concentration values obtained from ZetaView and mass-based analysis stems from limitations inherent to NTA, which is used by the ZetaView system. Nanoparticle Tracking Analysis (NTA) estimates particle concentration by analysing particle motion across video frames and normalising counts based on the scattering volume and size. However, at higher concentrations, particle overlap and trajectory ambiguity can compromise tracking accuracy. While dilution is commonly applied even below the manufacturer-specified upper limit of 10^9 particles/mL, approaching this threshold significantly increases the risk of underestimation due to tracking challenges. In our case, the sample concentrations were near this upper limit, making accurate quantification by NTA difficult. To address this, we employed a complementary mass-based approach, which is not affected by optical tracking limitations and provides a more reliable estimate of particle concentration in dense samples. The concentration of BNBs in the solution was far higher than the upper limit of the concentration that the machine could measure. Given that the upper limit concentration of DLS technology is lower than that of NTA, neither technology may be suitable for determining the concentration of highly concentrated nanobubbles.

Previous studies have noted the possibility of contamination by particles other than nanobubbles, which can occur during the generation process. We acknowledge this concern and have taken steps to minimize such contamination by using Milli-Q water and a closed generation system. However, techniques like DLS and NTA cannot definitively distinguish nanobubbles from other particles. To address this limitation, we incorporated a mass-based approach, which revealed a reduction in solution density, indicating the presence of low-density gas pockets consistent with nanobubbles. Crucially, the strong alignment between the experimentally observed rheological behaviour and our idealized, contamination-free simulations provides compelling evidence that the majority of particles are indeed nanobubbles. The system initially exhibits increased viscosity, which decreases under shear due to the disruption of nanobubbles. Notably, once the bubbles are destroyed, the viscosity remains low even if shear is reapplied, indicating that the shear-sensitive structures have been eliminated. This behaviour contrasts sharply with that of solid contaminants, which would remain intact under shear and continue to contribute to viscosity regardless of shear history. The irreversible drop in viscosity is therefore a strong indicator of the presence of nanobubbles rather than solid particles.

The size of the nanobubbles in the simulations is much smaller than those in the experiments, due to the inherent limitation of MD in the number of atoms that can be simulated. Perhaps, coarse-grained methods such as dissipative particle dynamics (DPD)70 could be considered in future to bridge this gap. Despite this size difference, the rheological experiments were in qualitative agreement with the simulations, where increased viscosity was observed at lower shear rates for nitrogen and air nanobubbles. However, the viscosity dropped to that of pure water with increasing shear rates. As demonstrated in the simulation, at higher rates, nanobubbles deform, coalesce, and most likely form larger bubbles released into the environment, leading to the viscosity reaching that of pure water. We also measured the zero-shear viscosity using an Ostwald viscometer. The results of this measurement showed reasonably good agreement with the rheological model we developed based on the simulation results.

Authorship contributions

Fankai Peng: Writing - original draft, Writing – review & editing, Visualization, Validation, Methodology, Investigation, Formal analysis, Data curation, Conceptualization. **Ahmad Jabbarzadeh:** Writing – review & editing, Validation, Supervision, Resources, Project administration, Methodology, Conceptualization.

Conflicts of interest

The authors declare no conflicts of interest.

Data availability

Data will be made available on request.

Acknowledgments

The authors acknowledge the use of the National Computational Infrastructure (NCI), supported by the Australian Government and accessed through the NCI Merit Allocation Scheme and the Sydney Informatics Hub HPC Allocation Scheme, supported by the Deputy Vice-Chancellor (Research), University of Sydney. The authors also acknowledge using the high-performance computational facility (Artemis) at the University of Sydney's Sydney Informatics Hub.

References

1. X. Wang, P. Li, R. Ning, R. Ratul, X. Zhang, J. Ma, *J. Clean. Prod.*, 2023, **426**, 139153.
2. V. S. Craig, M. P. Krafft, *Curr. Opin. Colloid Interface Sci.*, 2021, **55**, 101516.
3. L. Zhou, S. Wang, L. Zhang, J. Hu, *Curr. Opin. Colloid Interface Sci* , 2021, **53**, 101439.
4. D. V. Batchelor, F. J. Armistead, N. Ingram, S. A. Peyman, J. R. Mclaughlan, P. L. Coletta, S. D. Evans, *Curr. Opin. Colloid Interface Sci*, 2021, **54**, 101456.
5. B. H. Tan, H. An, C. D. Ohl, *Curr. Opin. Colloid Interface Sci*, 2021, **53**, 101428.
6. A. J. Atkinson, O. G. Apul, O. Schneider, S. Garcia-Segura, P. Westerhoff, Acc. Chem. Res., 2019, **52**, 1196-205.
7. A. Agarwal, W. J. Ng, Y. Liu, *Chemosphere*, 2011, **84**, 1175-80.
8. I. Levitsky, D. Tavor, V. Gitis. J, Water Proc. Eng., 2022, **47**, 102688.

9. Y. Wang, S. Wang, J. Sun, H. Dai, B. Zhang, W. Xiang, Z. Hu, P. Li, J. Yang, W. Zhang, Sci. Total Environ. , 2021, **800**, 149627.
10. Y. Zhou, F. Bastida, Y. Liu, J. He, W. Chen, X. Wang, Y. Xiao, P. Song, Y. Li, *J. Clean. Prod.*, 2022, **333**, 130050.
11. J. Wang, Q. He, K. Cao, B. Zhou, X. Niu, D. Wang, R. Chen, Z. Zheng, *Rhizosphere*, 2023, **28**, 100783.
12. Z. Gao, W. Wu, W. Sun, B. Wang, *Langmuir,* 2021, **37**, 11281-91.
13. S. A. Hewage, J. N. Meegoda, *Colloids Surf. A Physicochem. Eng. Asp.*, 2022, **650**, 129565.
14. Y. Lu, L. Yang, Y. Kuang, Y. Song, J. Zhao, A. K. Sum, *Phys. Chem. Chem. Phys.*, 2021, **23**, 27533-42.
15. J. Lei, D. Huang, W. Zhao, S. Liu, Y. Yue. *Int. J. Heat Mass Transf.*, 2024, **225**, 125407.
16. G. Senthilkumar, C. Rameshkumar, M. N. Nikhil, J. N. Kumar, *Appl. Nanosci.*, 2018, **8**, 1557-67.
17. S. Y. Kang, A. S. Sangani, H. K. Tsao, D. L. Koch, *Phys. Fluids*., 1997, **9**, 1540-61.
18. A. C. Rust, M. Manga, *J. Nonnewton. Fluid Mech.*, 2002, **104**, 53-63.
19. D. J. Stein, F. J. Spera, *J. Volcanol. Geotherm. Res.*, 1992, **49**, 157-74.
20. Y. Tasaka, T. Kimura, Y. Murai, *Exp. Fluids.*, 2015, **56**, 1867.
21. E. W. Llewellin, M. Manga, *J. Volcanol. Geotherm. Res.*. 2005, **143**, 205-17.
22. C. Mitrias, N. O. Jaensson, M. A. Hulsen, P. D. Anderson, *Rheol. Acta*, 2017, **56**, 555-65.
23. S. N. Hong, J. H. Ri, S. Y. Mun, C. J. Yu, *J. Mol. Liq.*, 2022, **367**, 120518.
24. F. Peng, A. Jabbrzadeh, *Phys. Rev. Let.*,2025 (under review).
25. W. B. Russel, W. B. Russel, D. A. Saville, W. R. Schowalter, *Colloidal Dispersions*. Cambridge University Press; 1991.
26. F. Morea, J. O. Agnusdei, R. Zerbino, *Mater. Struct.*, 2010, **43**, 499-507.
27. D. Katritsis, L. Kaiktsis, A. Chaniotis, J. Pantos, E. P. Efstathopoulos, V. Marmarelis, *Prog. Cardiovasc. Dis.*, 2007, **49**, 307-29.
28. V. B. Svetovoy, *Curr. Opin. Colloid Interface Sci.*, 2021, **52**, 101423.
29. T. Lyu, Y. Wu, Y. Zhang, W. Fan, S. Wu, R. J. Mortimer, G. Pan. *Sci. Total Environ.*, 2023, **895**, 165131.
30. A. Azevedo, H. Oliveira, J. Rubio, *Adv. Colloid Interface Sci.*, 2019, **271**, 101992.
31. J. Buescher, T. John, A. K. Boehm, L. Weber, S. M. Abdel-Hafez, C. Wagner, T. Kraus, M. Gallei, M. Schneider, *J. Drug Deliv. Sci. Tech.*, 2022, **75**, 103579.
32. K. Ohgaki, N. Q. Khanh, Y. Joden, A. Tsuji, T. Nakagawa, *Chem. Eng. Sci.*, 2010, **65**, 1296-300.
33. Y. Feng, A. Jabbarzadeh, *Phys. Fluids*, 2024, **36**.
34. J. J. Potoff, J. I. Siepmann, *AIChE J.*, 2001, **47**, 1676-82.
35. Z. Che, P. E. Theodorakis, *J. Colloid Interface Sci.*, 2017, **487**, 123-9.
36. LAMMPS Manual, TIP4P water model, LAMMPS Molecular Dynamics Simulator 2023, https://docs.lammps.org/Howto_tip4p.html, (accessed December 2023).
37. H. W. Horn, W. C. Swope, J. W. Pitera, J. D. Madura, T. J Dick, G. L. Hura, T. Head-Gordon, *J. Chem. Phys.*, 2004, **120**, 9665-78.
38. R. Span, E. W. Lemmon, R. T. Jacobsen, W. Wagner, A. Yokozeki, *J. Phys. Chem. Ref. Data*. 2000, **29**, 1361-433.
39. P. H. Bigg, *Br. J. Appl. Phys.*, 1967, **18**, 521.
40. J. Fischer, M. Wendland, *Fluid Phase Equilib.*, 2023, **573**, 113876.
41. M. P. Allen, D. J. Tildesley, Computer simulation of liquids. Clarendon: Oxford. 1987.
42. L. Martínez, R. Andrade, E. G. Birgin, J. M. Martínez, *J. Comput. Chem.*, 2009, **30**, 2157-64.
43. A. P. Thompson, H. M. Aktulga, R. Berger, D. S. Bolintineanu, W. M. Brown, P. S. Crozier, P. J. In't Veld, A. Kohlmeyer, S. G. Moore, T. D. Nguyen, R. Shan, *Comput. Phys. Commun.*, 2022, **271**, 108171.
44. M. S. Green, *J. Chem. Phys.*, 1954, **22**, 398-413.
45. R. Kubo, *J. Phys. Soc. Jpn.*, 1957, **12**, 570-86.
46. S. C. Cochran, *Mol. Phys.*, 1998, **93**, 117-22.
47. J. H. Irving, J. G. Kirkwood, *J. Chem. Phys.*, 1950, **18**, 817-29.
48. D. J. Evans, G. P. Morriss, *Phys. Rev. A*, 1984, **30**, 1528.
49. A. W. Lees, S. F. Edwards, *J. Phys. C: Solid State Phys.*, 1972, **5**, 1921.
50. R. Sun, W. Hu, Z. Duan, *J. Solution Chem.*, 2001, **30**, 561-73.
51. K. Ebina, K. Shi, M. Hirao, J. Hashimoto, Y. Kawato, S. Kaneshiro, T. Morimoto, K. Koizumi, H. Yoshikawa, *PLoS One*, 2013, **8**, e65339.
52. M. J. Assael, A. E. Kalyva, S. A. Monogenidou, M. L. Huber, R. A. Perkins, D. G. Friend, E. F. May, *J. Phys. Chem. Ref. Data*, 2018, **47**.
53. A. P. Markesteijn, R. Hartkamp, S. Luding, J. Westerweel, *J. Chem. Phys.*, 2012, **136**.
54. A. Einstein, *Ann. Phys.*, 1911, **34**, 591.
55. G. I. Taylor, *Proc. R. soc. Lond. Ser. A-Contain. Pap. Math. Phys. Character.*, 1932, **138**, 41-8.
56. I. M. Krieger, T. J. Dougherty, *Trans. Soc. Rheol.*, 1959, **3**, 137-52.
57. C. D. de Kruif, E. van Iersel, A. Vrij, W. B. Russel, *J. Chem. Phys.*, 1985, **83**, 4717-25.
58. R. Verberg, I. M. De Schepper, E. G. Cohen, *Phys. Rev. E*, 1997, **55**, 3143.
59. B. Cichocki, B. U. Felderhof, *J. Chem. Phys.*, 1988, **89**, 1049-54.
60. E. W. Lemmon, R. T. Jacobsen, *Int. J. Thermophys.*, 2004, **25**, 21-69.
61. S. Samavat, F. Carrique, E. Ruiz-Reina, W. Zhang, P. M. Williams, *J. Colloid Interface Sci.*, 2019, **537**, 640-51.
62. H. Zhang, Z. Guo, X. Zhang, *Soft Mat.*, 2020, **16**, 5470-7.
63. V. Rathee, A. Monti, M.E. Rosti, A.Q. Shen, *Soft Mat.*, 2021, **17**, 8047-58.
64. Y. Liu, Q. Zhang, R. Liu, *Rheol. Acta*, 2021, **60**, 763-774
65. J. Kestin, M. Sokolov, W. A. Wakeham, *J. Phys. Chem. Ref. data*, 1978, **7**, 941-8.
66. ZetaView Manual, ZetaView Evolution-Nanoparticle Tracking Analyzer, https://www.particle-metrix.com/pages/product-zetaview-evolution, (accessed May 2025).
67. Y. F. Chow, G. C. Maitland, J. M. Trusler, *J. Chem. Thermodyn.*, 2016, **93**, 392-403.
68. R. Span, E. W. Lemmon, R. T. Jacobsen, W. Wagner, A. Yokozeki. *J. Phys. Chem. Ref. Data*, 2000, **29**, 1361-433.
69. C. Vega, E. de Miguel. *J. Chem. Phys*., 2007, **126**, 154707.
70. A. Moshfegh, A. Jabbarzadeh, *Soft Mater.*, 2015, **13**, 106-117.

View Article Online
DOI: 10.1039/D5NR03035H

Data Availability Statement

All data supporting the findings of this study are included in the manuscript. The simulation parameters, modelling details, and experimental results are provided to ensure full reproducibility of the work.